RICE UNIVERSITY

Plasmonic modulation of fluorescence point spread functions reveals underlying properties of quantum emitters
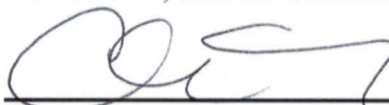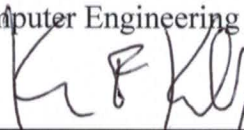
by

Rashad Baiyasi

A THESIS SUBMITTED
IN PARTIAL FULFILLMENT OF THE
REQUIREMENTS FOR THE DEGREE

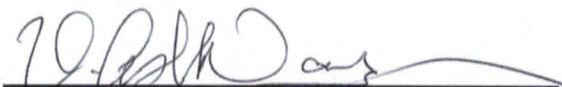## Master of Science

APPROVED, THESIS COMMITTEE

Christy F. Landes, Chair
Professor, Chemistry & Electrical and
Computer Engineering

Kevin F. Kelly
Associate Professor, Electrical and
Computer Engineering

Palash Bharadwaj
Assistant Professor, Electrical and
Computer Engineering

Ashok Veeraraghavan
Associate Professor, Electrical and
Computer Engineering & Computer
Science

HOUSTON, TEXAS
April 2018

ABSTRACT

Plasmonic modulation of fluorescence point spread functions reveals underlying properties of quantum emitters

by

Rashad Baiyasi

Plasmonic nanostructures offer a wealth of novel optical properties but optimization of their structure-function relationship with superlocalization techniques is hindered by the modification of point spread functions (PSFs) due to nanoantenna effects. The biasing of PSFs towards nanoparticle centers has been widely investigated, while the biasing of PSFs away from nanowires (NWs) has not received much attention in literature. I investigate the localization bias and extra localizations observed in wide-field fluorescence microscope movies collected by collaborators of Alexa 647 dye labeled Ag nanowires imaged under remote excitation. I introduce and focus on two main classes of abnormal PSFs: single-lobed PSFs exhibiting a variable localization bias based on position around the nanowire (NW) and bi-lobed PSFs occurring near the top edge of the NW. Finite-difference time-domain simulations show that the localization bias for these two populations form distinct distributions for NW diameters below 300 nm. The experimental apparent width of these NWs suggests a larger population of bi-lobed PSFs due to heterogeneous emission of Alexa 647 dependent on dye position. I also present a novel fitting method for these abnormal PSFs using Hermite-Gaussian basis functions and show that dipole emitter orientation is encoded in multi-lobed PSFs.

Acknowledgments

I would like to thank my advisor Dr. Christy F. Landes for her support and motivation during the course of my research, and for always encouraging me to look deeper at the underlying phenomenon at the intersection of imaging and plasmonics.

Thank you to Dr. Kevin Kelly, Dr. Palash Bharadwaj, and Dr. Ashok Veeraraghavan for serving on my thesis committee, for the knowledge they have given me inside and outside of the classroom, and for their insights and comments.

I would like to thank my fellow lab members in the Landes and Link research groups, as well as my cohorts in the Electrical and Computer Engineering department, for their support in research and life in general. I'd like to especially thank Thomas Heiderscheit and Caitlin McCowan for keeping me going when things were tough.

Finally, I'd like to thank my family, who believed in me and pushed me to always do my best. Thank you for your support and love throughout my academic career.

Contents

List of Figures

List of Equations

Nomenclature

PSF	Point spread function
NP	Nanoparticle
NW	Nanowire
SEM	Scanning electron microscope
FDTD	Finite-difference time-domain (simulation)
STORM	Stochastic optical reconstruction microscopy
PALM	Photo-activated localization microscopy
PAINT	Point accumulation for imaging in nanoscale topography

Chapter 1

Introduction

1.1. A superlocalization approach to studying nanocatalysts

Metal nanoparticles (NPs) are promising candidates for a new generation of stable, efficient, and low-energy catalysts [1, 2] due to their unique optical properties [1, 3-5]. Incident light excites collective oscillations of the valence electrons, referred to as surface plasmons, which scatter into the far field or decay through various pathways [6, 7]. Catalysts formed from various plasmon-supporting metals have been studied [2, 5, 8, 9], as have more complex structures that combine the light harvesting effects of plasmonic NPs with non-plasmonic catalysts [10-15]. Evidence shows that they display high selectivity [10] and the capacity to facilitate interactions otherwise thought "impossible" [2, 16]. The efficiency of metal nanocatalysts has been shown to vary dramatically with not just size but also shape [17]. Edges and defects form sites with higher catalytic activity due to lower

coordination saturation of the crystal facets. Experiments on Au nanorods [18] and nanoplates [19] have measured novel intra-particle catalytic activity *in situ* using superlocalization and tracking of individual fluorogenic reactions. Using superlocalization microscopy to track individual catalytic reactions allows one to extract structural information, which could provide insight into the structure-activity relationship and optical tracking of NP reshaping. This superlocalization approach is the most powerful method to precisely identify and localize the sites of individual reactions, but such techniques depend heavily on well-behaved point spread functions (PSFs) to yield accurate fluorescent emitter positions [20-23].

1.2. Superlocalization of quantum emitters

Localization of a particle or emitter with sub-diffraction limit precision is referred to as superlocalization. Superlocalization microscopy is a powerful tool for imaging below the diffraction limit of light, but has been shown to fail when applied to metal NPs [20, 24-27]. Superlocalization microcopy has already found numerous applications in the field of biological imaging [28-32], but using it to study metal surfaces and nanostructures provides more than just superresolution images. Superlocalization provides the ability to probe electromagnetic hotspots [33], protein monolayer formation [34], catalytic reactivity patterns [18, 35-37], and regimes of fluorescent enhancement and quenching [38, 39]. However, experimental and simulated data reveals that we often cannot accurately localize emitters near metal NPs [20, 24-27].

The key concepts that enable superlocalization are the prior knowledge that there is only one emitter in an 'on' state in a diffraction-limited region, and that the PSF can be used to extract the precise position of the emitter [21, 22]. Superlocalization microscopy techniques such as STORM [40], PALM [41], and PAINT [42, 43] use stochastic excitation or reversible binding of fluorescent species to vary the density of active emitters so that only a sparse subset are 'on' at any given time. Recording images of multiple sparse subsets of emitters allows the final super-resolution image to be reconstructed from localizations determined in each frame. Quantum dipole emitters, such as fluorescent dyes or quantum dots, can be switched between 'on' and 'off' states in several ways.

Obtaining fluorescent localizations with sub-diffraction limit precision requires either fitting of the PSF [21-23] or taking advantage of some other property (such as radial symmetry [44]). The PSF is the blur returned by an imaging system in response to an isotropic point source of photons, spread out with a characteristic width $\approx \lambda/(2 \cdot NA)$, where λ is wavelength and NA is numerical aperture [21, 22]. While the width of the PSF is limited by the diffraction limit of light, the uncertainty in the estimated localization varies as the inverse of the square root of the number of collected photons [45], and typical experimental conditions give localization precisions of ~20 nm. The 2D paraxial wide-field fluorescence microscope PSF is the Airy disk [46] and is often approximated as a 2D Gaussian for superlocalization algorithms due to its accuracy and computational simplicity [23]. Not all superlocalization techniques require fitting the PSF to a model [23, 44], but a well-behaved, or at least well-understood, PSF is vital.

1.3. Superlocalization of Alexa 647 near Ag nanowires

Experimental wide-field fluorescence movies and scanning electron microscope (SEM) images of Alexa 647 labeled Ag nanowires (NWs) for use in my research were obtained from collaborators in the Hofkens group [20]. NWs were functionalized with Alexa 647 dye with a bulky bioconjugation as a linker, maintaining a distance of ~10 nm between dye and NW surface [20]. NW-dye complexes were drop cast onto coverslips and movies of ~2000 frames were recorded with the NWs under remote excitation [20]. Remote excitation of fluorophores was accomplished by using a polarized (longitudinal, lateral, or circular relative to the NW axis) 632.8 nm He-Ne laser focused on one end of the NW to launch propagating surface plasmon polaritons [20]. Alexa 647 dye molecules were excited by the evanescent field extending outside the NW and fluorescent emission was projected into the far field [20]. I calculated localizations frame-by-frame using the radial symmetry method [44] to approximate PSF lobe positions with the understanding that localizations were not the true Alexa 647 dye positions [20].

1.4. Localization bias near plasmonic nanostructures

Plasmonic NPs have been shown to act as nanoantennas [26, 47], altering the PSF of fluorescent dyes so that traditional superlocalization techniques provide inaccurate localizations [48-50]. Imaging fluorescent events on plasmonic NPs is complicated by the shifting and reshaping of the PSF due to coupling effects, such

that the localization is significantly biased away from the actual emitter position [20, 25, 49, 50]. Despite the theoretically improved localization precision that fluorescent enhancement from plasmonic NPs provides, this localization bias must be addressed to obtain accurate localizations [50].

Ag NWs are a powerful tool for confining and guiding electromagnetic radiation below the diffraction limit of light and could prove useful in more complex antenna-reactor structures for catalysis, but when a standard PSF model is used to localize fluorescent labels adsorbed to the structure, the distribution of localizations overestimates the NW diameter by several tens of nanometers [20]. To determine why dye labels on the NW were being localized outside of the NW support, Su et al. simulated the NW-dye system to reveal that PSFs were not only shifting, but also splitting into abnormal, multi-lobed PSFs [20]. This means that a single emitter can result in multiple blurs, or lobes, in the image plane, breaking the standard assumption of superlocalization that each blur is a PSF centered on a single emitter. Coupling between NWs and quantum emitter such as quantum dots or fluorescent dyes has been extensively studied using a variety of techniques [51-57], but to the best of our knowledge no method has been proposed to approach the fitting of these abnormal PSFs, which is a challenge that must be addressed if superlocalization microscopy is to be used to extract nanoscale structure or reactivity sites. A necessary initial step for superlocalization under these conditions is the classification of abnormal PSFs so that, for example, two single-lobed PSFs are not localized as a single, two-lobed PSF. I have developed a framework and identified

optimal systems for the classification of these abnormal PSFs by examining their size and shape in the context of dipole emitter geometry and Ag NW diameter.

1.5. Scope of this thesis

I have simulated multi-lobed PSFs using the finite-difference time-domain (FDTD) method for uniformly distributed dipole emitter positions and orientations on a range of NW diameters and classified them according to their lobe structure. By superlocalization of Alexa 647 adsorbed to Ag NWs I have found evidence of a larger population of multi-lobed PSFs than uniformly distributed dyes would generate. This increased occurrence rate of multi-lobed PSFs is a main source of the significant overestimation of thinner NW diameters by superlocalization, as the different classes of PSFs I simulated occur with different frequencies and contributing differently to the overestimation of NW diameter. I have identified that NWs with diameters in the range of 200 to 300 nm are best suited to distinguish between different PSF classes. As an example of how the fitting of identified multi-lobed PSFs can provide more than just sub-diffraction limited localizations, I have developed and employed a novel Hermite-Gaussian basis to fit simulated multi-lobed PSFs and extract the underlying orientation of the associated dipole emitters. This new method opens the door for future superlocalization of dyes on metal substrates that produce non-Gaussian PSFs.

Chapter 2

Simulation of Multi-Lobed Point Spread Functions

2.1. Simulation of electric near fields

Using Lumerical FDTD Solutions, emission patterns of a dipole source near pentagonal cross-section Ag NWs were calculated that mimics the fluorescent radiation from a molecule close to the NW. The small dipole was located 10 nm above the NW surface to simulate the Alexa 647 dye and bulky bioconjugation linker. The dielectric function of silver was extracted from Johnson & Christy [58], while the background index of refraction was set to 1.33. The glass substrate, with index of refraction of 1.52, was placed below the NW with a gap to simulate the even NW coverage by the dye and linker. A monitor in the substrate recorded the electric field for generating simulated PSFs using the plane wave spectrum method.

2.2. Parallelization of the far field projection

The electric field data taken from the frequency domain profile monitor in Lumerical served as the input at the focal plane of the optical system. In order to model the effects of the objective lens, I used the *farfieldexact* script built into Lumerical FDTD Solutions. This function projects complex vector fields out to specified points in space - in my case, I projected onto a hemisphere of radius 1 m to simulate an infinite distance. Propagation to the far field projects the electric field to the Fourier plane, where each point is associated with a plane wave from the angular spectrum representation of the near field distribution [59].

In order to generate the ~20,000 simulations I used to study a range of NW diameters and uniformly distributed dipole emitter, parallelization was an important step. To accomplish this I used 10 nodes on the DAVinCI cluster at Rice University (12 cores per node at 2.83 GHz). The Lumerical FDTD Solutions Maxwell's equations solver engine used to calculate the near field distribution supports parallelization but the scripting language needed for far field projection does not. Through a combination of bash scripts and the stream editor Sed, I developed a process to parse large sets of near field data from the Lumerical engine and submit them to individual cores on the supercomputer. Due to the large number of simulation files I was projecting, this basic form of parallelization resulted in a speedup of ~16x. This allowed me to simulate thousands of dipoles in a matter of hours rather than days, and gave me the flexibility to quickly add to my dataset when needed.

2.3. Simulation of PSFs

The angular spectrum representation is a powerful tool for calculating the propagation of complex electromagnetic fields [59, 60]. Using this method, 2-dimensional (2D) Fourier transforms take the place of lenses, while propagation through space after the objective lens is modeled as multiplication by a phase-shift factor. It is an interesting fact that lenses actually perform 2D Fourier transforms on incident light - the lens performs a coordinate transformation from spatial to angular coordinates [60].
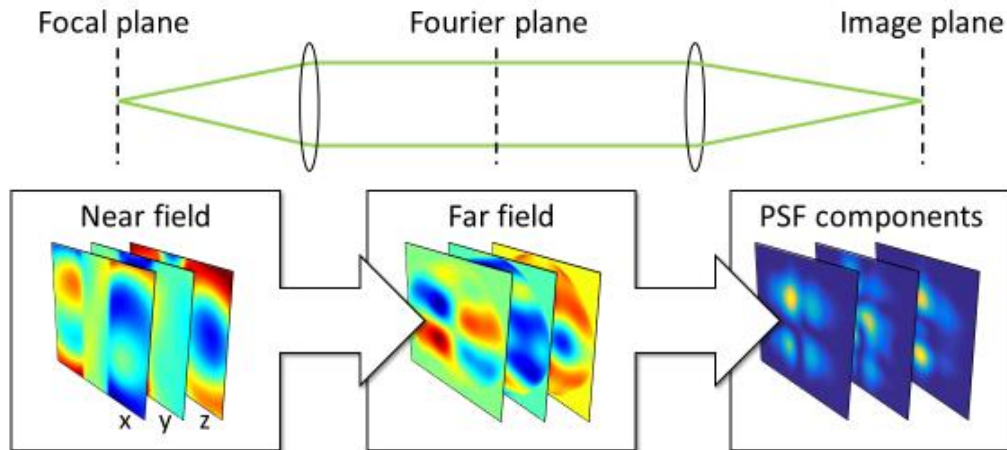
Figure 2.1. Projecting near field simulation data to the image plane by the angular spectrum method. Simulated near field data is recorded by the monitor in Lumerical FDTD Solutions acting as the focal plane. Far field projection mimics the role of the objective lens, projecting the components of electric field to the Fourier plane. A 2D Fourier transform acts as the tube lens, projecting from the Fourier plane to the image plane, where the components are combined into a positive-real valued intensity map, or PSF. Near and far field are depicted as the real values of the complex electric field components, while the PSF components are shown as intensity maps.

Each complex-valued component of the electric field on the far field hemisphere was propagated to the image plane using a 2D Fourier transform, resulting in the PSF components shown in Figure 2.1. Pixel sizes for simulated images were calculated using the relation $p_2=(m_1\lambda)/(2m_2NA)$ for the emission wavelength λ, the numerical objective NA, and the number of pixels used in the far field and the image plane (m_1 and m_2, respectively) [21]. Several example PSFs are shown in Figure 2.2. The PSFs show multi-lobed and single-lobes structure depending on the position and orientation of the dipole source, here simulating the transition dipole of a fluorescent label [20]. Figure 2.2c-f shows how rotation or translation of the dipole source causes reweighting of relative lobe intensities and shifting of lobe positions. Since lobes are not generally symmetric, the position of each lobe for use in quantifying localization bias is calculated using the maximum intensity points of high-resolution simulated PSFs.
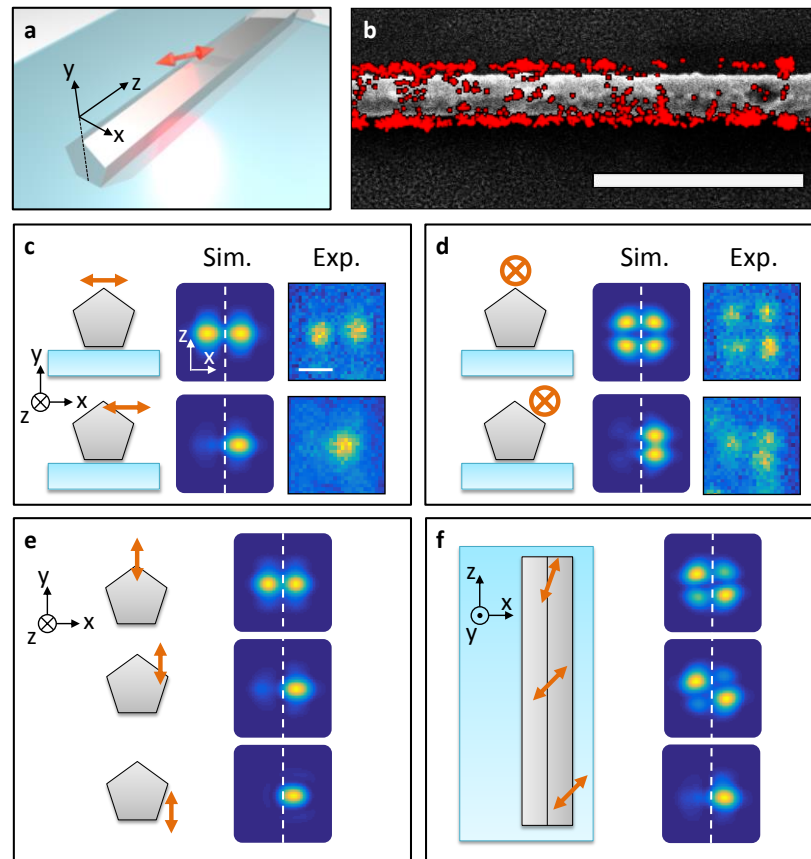
Figure 2.2. Multi-lobed emission patterns are observed for Alex 647-labeled Ag NWs. (a) Pictorial representation of a pentagonal cross-section Ag NW on a substrate labeled with a fluorescent dye. The orange arrow represents the transition dipole of an Alexa 647 dye modeled as a dipole emitter in simulation. The orientation and position of the transition dipole determines the properties of PSFs. (b) Sample super-resolution reconstruction of dye-labeled Ag NWs overlaid on SEM. Direct localization of fluorescent spots shows strong bias towards the NW edges. Scalebar 2 μm. (c-f) Varied transition dipole orientation and position with associated PSFs. (c-d) Effect of shifting the dipole away from the apex reweights the relative lobe intensities as seen in simulation (middle columns) and experiment (right columns, scalebar 500 nm). (e) Simulated PSFs for dipole oriention along the optical axis. (f) Rotated and shifted dipoles shows more complex reweighting behavior in PSFs (top-down view of NW). Dotted line indicates the NW axis in all simulated PSFs.

Chapter 3

Quantifying plasmon-induced localization bias

3.1. Overestimation of dye-labeled Ag NW diameter

The apparent width of Ag NWs from superlocalization of Alexa 647 dye labels consistently overestimates the diameter by ~100 nm for various NW samples. Figure 3.1a-b shows the SEM image and localization map for a sample NW with a diameter of ~400 nm. The distribution of localizations in Figure 3.1b can be visualized as displacements from the NW axis, shown as a histogram in Figure 3.1c. I define the apparent width of the NW as the distance between the peaks of this distribution. For localizations accurately representing emitter positions, the apparent width is ~50 nm less than the NW diameter. However, across a wide range of NW diameters the apparent width overestimates the NW diameter as shown in Figure 3.1d. The blue circles show the apparent width of Ag NWs from PSFs calculated from FDTD simulations. Vertical error bars/regions for experiment and simulation are calculated as the standard deviation of the distribution about the peaks, calculated using a histogram as show in Figure 3.1c. Experiment and

simulation agree for NW diameters between 400 and 700 nm but diverge for

thinner NWs. For a NW with ~200 nm diameter, simulations predict an apparent

width within 20 nm of the NW diameter, while the experimental apparent width is

~150 nm greater than the diameter. The source of the apparent width

overestimation can be traced back to the different abnormal PSFs observed in

simulations.
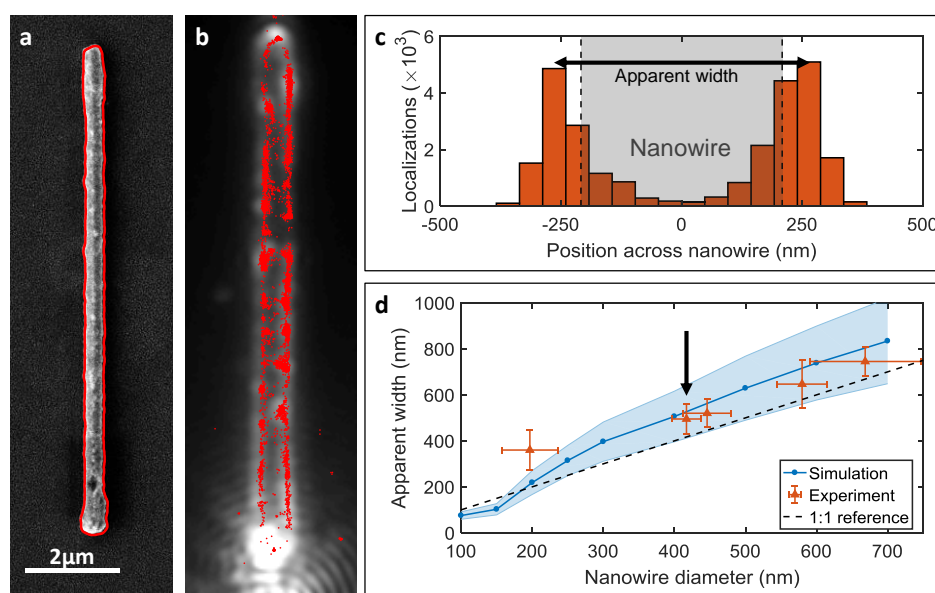
Figure 3.1. The apparent width of pentagonal cross-section NWs imaged via superlocalization of fluorescent emitters overestimates the NW diameter by approximately 100 nm. Experimental data collected by collaborators in the Hofkens group [20]. (a) SEM image of a representative Ag NW, with the detected edge outlined in red. (b) Average wide-field fluorescent image of the same NW as in (a) recorded as a 2000 frame movie, with localizations calculated for each frame using the radial symmetry method[44] and shown as red points. Scale is given by the scalebar in (a). (c) Localization events across the width of the NW (gray region). The apparent width is defined as the distance between the peaks of the distribution of localizations. (d) Apparent widths as a function of NW diameter for a set of five NWs (red triangles) are compared to simulation (blue circles). The black arrow indicates the data

point formed by the sample NW shown in (a-c). Dashed black line is a 1:1 reference showing the actual NW diameter. Vertical error bar/region show the standard deviation of localizations around the peaks (as shown in (c)). Horizontal experimental error bars the standard deviation in the SEM widths along each NW. Apparent width diverges for NWs with diameter ~200 nm with simulated apparent width predicting no overestimation while experiment shows the greatest overestimation.

3.2. Classification of PSFs

I found that the apparent width overestimation shown in Figure 3.1d originates from different contributions from classes of complex PSFs for dipole emitters near Ag nanowires. I classified PSFs as single-lobed, two-lobed oriented perpendicular to the nanowire axis, two-lobed oriented parallel, and four-lobed. A representative sample of PSFs were calculated for each nanowire using 2000 uniformly distributed dipole emitter positions and orientations in the simulation space. As summarized in Figure 3.2, the most common class of PSFs are single-lobed and two-lobed oriented perpendicular to the nanowire, the latter of which I will refer to as bi-lobed PSFs for brevity. Single-lobed PSFs contribute to apparent width overestimation though the biasing of the PSF away from the nanowire axis, while bi-lobed PSFs contribute through the separation between the two lobes. While single- and bi-lobed PSFs overestimate the nanowire to a similar degree for nanowire diameters above 400 nm, they diverge for thinner nanowires. The source of this discrepancy is the different contributions of single- and bi-lobed PSFs to apparent width and will be discussed in greater details in the next section.
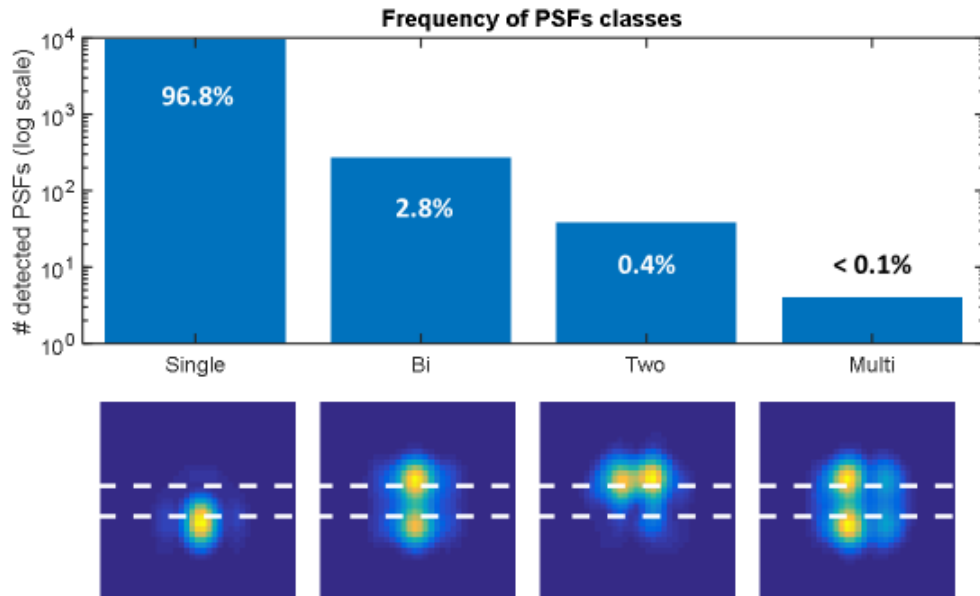
Figure 3.2 – Classification of PSFs. 20,000 PSFs for uniformly distributed dipole emitters were simulated and classified as one of four types of PSFs. PSFs with only one lobe are classified as single-lobed. PSFs with two lobes are split between those with lobes oriented perpendicular to the NW axis (bi-lobed) and those oriented parallel (two-lobed). PSFs with more than two lobes are classified as multi-lobed. The histogram shows the relative occurances of each class of PSF (log scale).

3.3. Contribution of single- and bi-lobed PSF to apparent width

Simulated apparent width decomposed by PSF class demonstrates that at NW diameters < 300 nm bi-lobed PSFs yield a much greater overestimation than single-lobed PSFs. The apparent width for single-lobed and bi-lobed PSFs are shown in Figure 3.3a as a function of NW diameter. Their apparent widths agree in an overestimation of ~100 nm for NW diameters > 400 nm, but they diverge for thinner NW. The separation between single- and bi-lobed apparent widths simulated for a 200 nm diameter NW is similar to the disagreement between

simulation and experiment shown in Figure 3.1d. For the 200 nm diameter NW, the single-lobed apparent width is within 20 nm of the NW diameter and the bi-lobed apparent width overestimation is ~200 nm. The decrease in apparent width overestimation for single-lobed PSFs at low NW diameters can be traced to the decrease in localization bias with decreasing NW diameter. The bias of single-lobed PSFs depends on the NW diameter and where emitters are located around the NW. As shown in Figure 3.3b, the bias in single-lobed PSF localization decreases more dramatically from 400 to 200 nm than from 600 to 400 nm. The difference in apparent width overestimation can also be seen in Figure 3.3c, where the single-lobed and bi-lobed PSFs for a 400 nm diameter (right column) appear the same distance outside the NW diameter, while for a 200 nm diameter NW (left column) the single-lobed PSF is closer to the true NW edge than the bi-lobed PSF. One would expect that the simulated apparent width from all PSFs would fall somewhere between these two values, but it in fact precisely matches the single-lobed trend. This is due to the fact that more than 95% of PSFs are single-lobed for simulations of uniformly distributed dipole emitters (Figure 3.2).
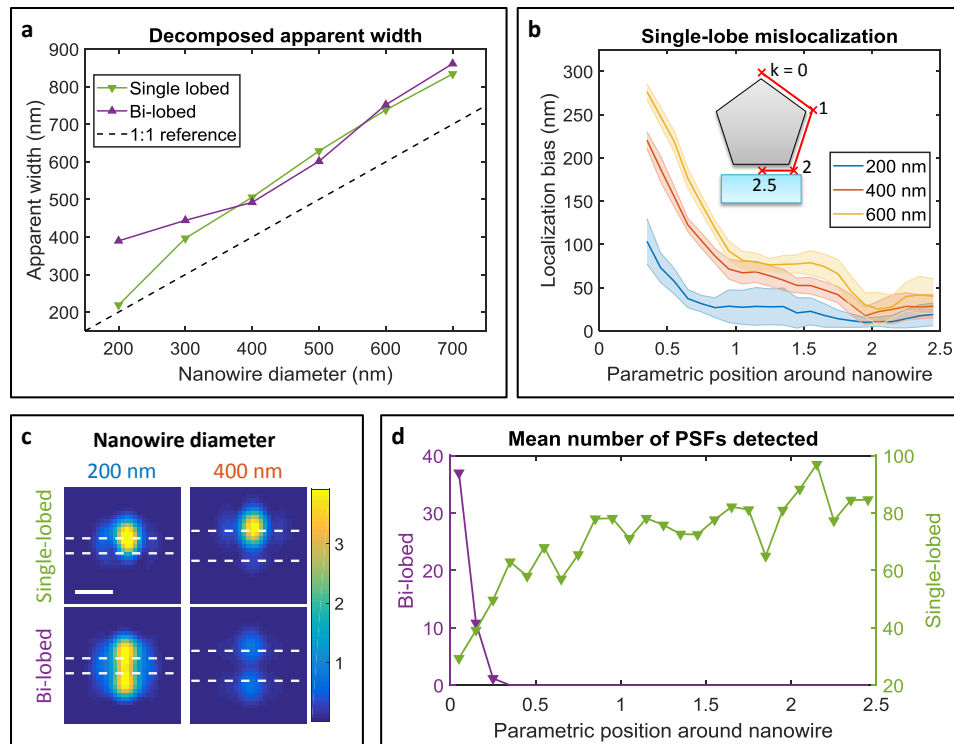
Figure 3.3. The relative occurrence rate of PSFs favors single- over bi-lobed PSFs. (a) Apparent width decomposed in terms of single- and bi-lobed PSFs diverge for smaller NW diameters. (b) Mislocalization of single-lobed PSFs as a function of parametric dipole position k (inset) for different NW diameters. Localization bias is not shown for k < 0.35 due to infrequency in single-lobed PSF occurrence. (c) PSFs simulated for two dipole geometries (resulting in single- and bi-lobed PSFs) and two different NW diameters. The intensity of the bi-lobed PSFs decreases more dramatically with increasing NW diameter than for single-lobed PSFs. Colorbar and scalebar of 500 nm is shared between the PSFs. (d) Number of bi-lobed and single-lobed PSFs detected around a NW. Bi-lobed PSFs only occur near the apex of the nanowire ($k = 0$) while single-lobed dominate otherwise.

Bi-lobed PSFs occur less frequently than single-lobed PSFs in simulations

with uniformly distributed dipole emitters due to the dipole emitter configurations

that can produce them and their relative intensity. As shown in Figure 3.3d, bi-lobed

18

PSFs only occur for dipole emitters in a narrow region around the apex of the NW. Single-lobed occurrence is at a minimum at the nanowire apex, but aside from this region the rest of the NW is dominated by single-lobed PSFs. The occurrence rate of bi-lobed PSFs decreases with increasing NW diameter because decreasing bi-lobed PSF intensity hides them in noise at larger NW diameters. This is demonstrated in Figure 3.3c, which shows four PSFs generated by two different dipole emitter geometries (resulting in single- or bi-lobed PSFs) simulated for NW diameters of 200 and 400 nm. As NW diameter is increased, the bi-lobed PSF intensity decreases more dramatically than single-lobed. With lower intensities, these bi-lobed PSFs are less likely to be detected over noise. Bi-lobed PSF fraction also drops for NWs below 300 nm, as the spread of the lobes leads to overlap and can result in misidentification as a single lobe.

3.4. Enhanced bi-lobed PSF expression in experiments

Experimental apparent width for ~200 nm diameter NW predicts a higher relative occurrence of bi-lobed PSFs than is obtained from uniformly distributed dipole emitters in simulation. The divergence in apparent width for simulation and experiment shown in Figure 3.1d is similar to the different apparent widths calculated for only single-lobed and only bi-lobed PSFs as is shown in Figure 3.3a. As described above, single-lobed PSFs dictate the apparent width for the overall simulation resulting in less than 20 nm overestimation of NW diameter. In contrast, the experiment more closely resembles the apparent width shown by bi-lobed PSFs. This suggests that the true distribution of PSFs has a higher occurrence of bi-lobed

19

PSFs than from the uniformly distributed dipole emitters used in simulation. The

effect of increasing the percentage of bi-lobed PSFs on the simulated apparent width

is shown in Figure 3.3d. The average apparent width for 100 trials increases for

between 20% and 30% bi-lobed PSFs, levelling off on either side of this region. The

simulated apparent width only comes into agreement with the experimental result

in Figure 3.1d (orange line) for > 30% bi-lobed PSFs compared to the 5% found for

uniformly distributed dipoles.
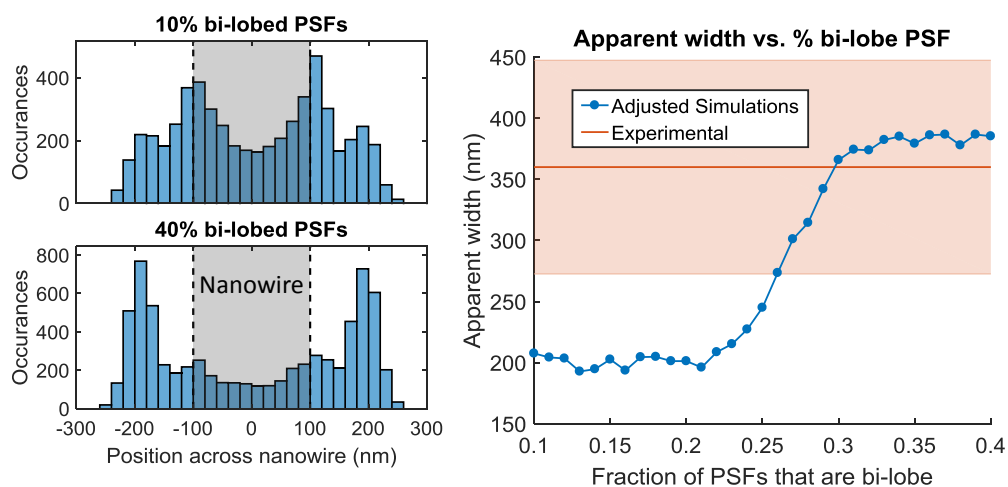
Figure 3.4 – Apparent width varies with occurrence rate of bi-lobed PSFs for a simulated 200 nm diameter NW as compared to experiment. Agreement with experiment is reached when ~30% of PSFs are bi-lobed. Sample histograms of localizations across the NW for 10% and 40% bi-lobed PSFs show different apparent widths for the same NW diameter (grey).

Bi-lobed PSFs may be expressed more frequently under experimental

conditions due to inhomogeneity in dye coverage or the spatial distribution of

plasmon near fields. As they only occur at the apex of the NW, preferential binding

of the biotin-terminated poly(ethylene glycol) to the NW edges due to crystal facets, defects, or crowding effects, would increase the relative occurrence of bi-lobed PSFs. Furthermore, the excitation of dyes through propagating surface plasmon polaritons will result in fluorescent enhancement in the regions around the NW corners where the electric field is most tightly confined. The FDTD simulations performed herein uses a constant dipole emission rate, while the proximity of various plasmonic NP features have been shown to drastically enhance or quench fluorescence [27, 33, 61, 62]. Further experiments are needed to distinguish between these two effects – for example, wide-field excitation of a dye-labeled, non-plasmonic NW could use three-dimensional superlocalization methods [21, 63-65] to examine only the preferential binding effects.

The optimum pentagonal cross-section Ag NW-Alexa 647 system to study for classification of experimentally measured multi-lobed PSFs should utilize NW diameters between 200 and 300 nm to maximize the differences between single- and bi-lobed PSFs. At lower NW diameters, bi-lobed PSFs merge into single blurs due to the diffraction limit. Meanwhile, at larger NW diameters the similar apparent width (Figure 3.3a) means that the separation between two blurs cannot be used to classify them as a single bi-lobed PSF. For NW diameters that support bi-lobed PSFs, there is some probability that two single-lobed PSF expressing dipoles may be positioned close to each other. Figure 3.5 shows how this can result in what appears to be a bi-lobed PSF. If the distribution of single- and bi-lobed PSFs have similar apparent widths, a more sparse set of active emitters is needed in each frame to decrease the likelihood of false identification of bi-lobed PSFs. Under the optimal

conditions described above, candidate PSF identification can incorporate lobe separation as a way to lower the false-positive rate in bi-lobed PSF classification. Future experiments characterizing the dipole emitter-NW interaction is benefited by the relatively high occurrence rate of bi-lobed PSFs. As opposed to other emitter-NP systems which only produce biased single localizations, there is information encoded into the extra lobes present in the system studied here. While no methods have been presented in the literature on how to treat such multi-lobed PSFs, the Hermite-Gaussian model presented below shows how one can extract fluorescent transition dipole moment orientations from bi-lobed PSFs.
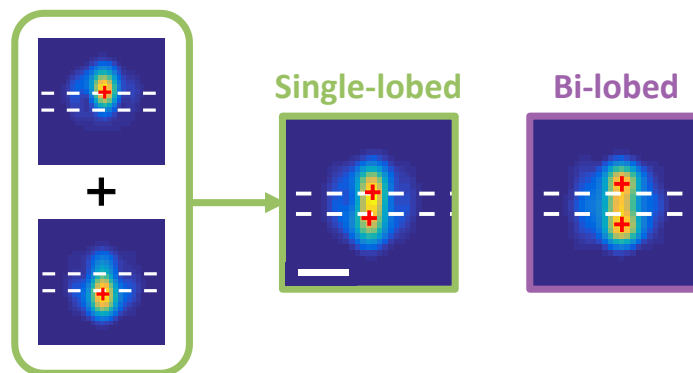
Figure 3.5 – False bi-lobed PSFs can be formed if two active dipole sources forming single-lobed PSFs occur on opposite sides of the NW. Red crosses represent the lobe localization.

<p style="text-align: right;">Chapter 4</p>

Fitting multi-lobed PSFs

4.1. Multi-lobed PSFs present a novel problem for modelling

I developed a method for fitting of multi-lobed PSFs using a Hermite-Gaussian (HG) basis to quantitatively analyze multi-lobed PSFs. My method of modeling polarized components of multi-lobed PSFs as a linear combination of the Hermite-Gaussian functions is an example of how one might approach the fitting of novel PSFs. The analysis of apparent width and its dependence on PSF class presented above is useful, but a functional method is needed to better characterize and fit multi-lobed PSFs. Localization with a standard technique (such as Gaussian fitting or radial symmetry) could serve as a preprocessing step in which individual blurs are grouped together into candidate multi-lobed PSFs. The relative position and intensity of the candidate lobes provide features to describe the PSFs but due to the non-Gaussian profiles of lobes, a functional PSF model would be preferable for robust fitting of multi-lobed PSFs.

23
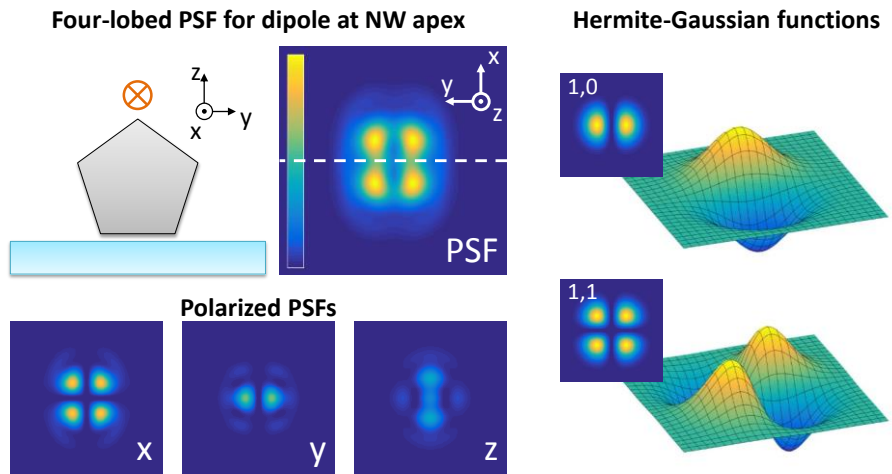
Figure 4.1. HG functions form a basis for a multi-lobed PSF model. Simulated PSF and polarized PSFs for a dipole emitter at the apex of a NW and two HG functions which look similar to the x- and y-polarized PSFs.

The variety of PSFs formed by dipole emitters near NWs presents difficulties for fitting since a simple model in the same vein as the Gaussian or Airy PSF model cannot assume such varied forms. While a basis for fitting could be constructed by feeding a many PSFs into a machine learning algorithm, the resultant basis would be unique to the simulation parameters, limited by the training data, and would lack any physical significance. However, a potential basis for fitting PSFs can be seen by inspecting polarized PSFs. Figure 4.1 shows the similarity between the polarized components of a simulated PSF and the intensity maps of the (1,0) and (1,1) HG functions.

4.2. The HG basis for PSFs fitting

The HG functions are described by

$$E_{nm}(x, y, z) = E_0 \frac{w_0}{w(z)} \cdot H_n\left(\sqrt{2}\frac{x}{w(z)}\right) e^{-\frac{x^2}{w(z)^2}} \cdot H_m\left(\sqrt{2}\frac{y}{w(z)}\right) e^{-\frac{y^2}{w(z)^2}} \cdot e^{\wedge}$$

$$-i\left(kz - \Phi(m, n, z) + \frac{k(x^2 + y^2)}{2R(z)}\right)$$

Equation 4.1

where $w(z) = w_0\sqrt{1 + \frac{z}{z_R}}$ is the beam waist or radius, w_0 is the beam waist at the

focus, $R(z) = z\left(1 + \frac{z_R^2}{z}\right)$ is the radius of curvature, $z_R = \frac{\pi w_0^2}{\lambda}$ is the Rayleigh length

for wavelength λ, and $\Phi(m, n, z) = (1 + n + m)\arctan\left(\frac{z}{z_R}\right)$, where m and n are

integers denoting the different HG modes.

The first few HG functions are shown in Figure 4.2a. The HG functions are a set of
orthogonal complex-valued solutions to the paraxial approximation of the wave
equation [66, 67]. They display rectangular symmetry and form a complete, infinite
basis for the space of square integrable complex functions [68]. The HG functions
appear in the analytical solution for strongly focused laser beams [59] and have
been used as a model for extracting orientation of fixed dipoles in free space [66].
The (0,0) mode is the common Gaussian beam and the higher-order modes are
inhomogeneous solutions to the paraxial wave equation with Cartesian symmetry.

While the polarized PSFs for certain orientations almost directly match specific HG

functions as in Figure 4.1, other PSFs that do not directly match the HG basis

functions can be fit by a linear combination of weighted basis functions, as is shown

in

Figure 4.2b for a dipole emitter rotated 20° off the NW axis in the image

plane.
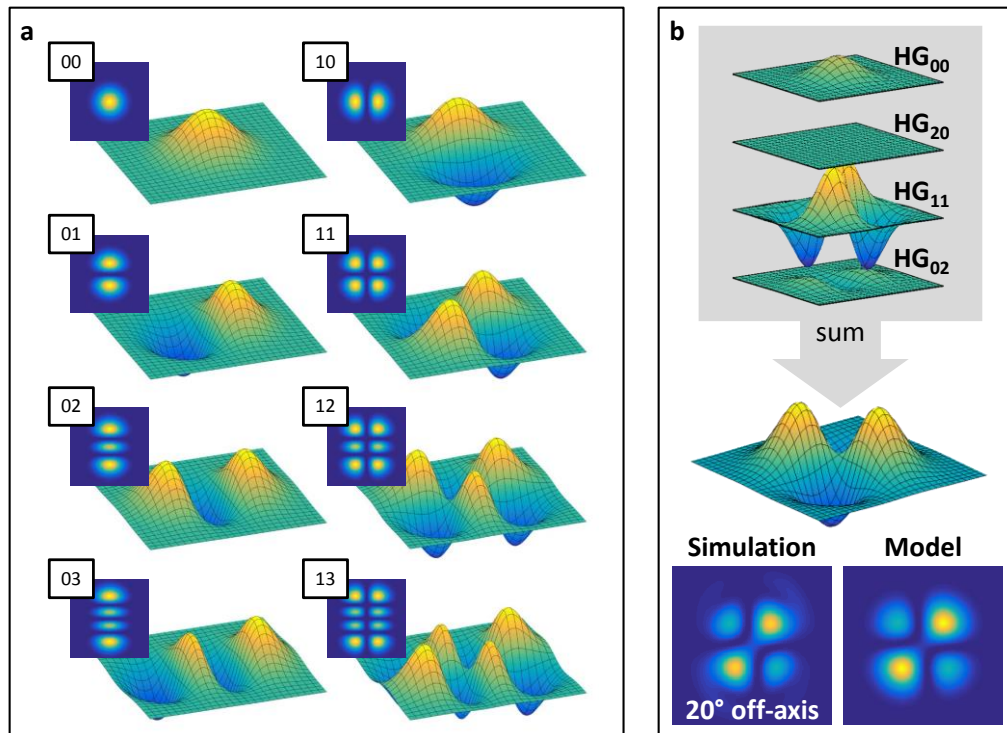
Figure 4.2. (a) Representative HG functions, shown as real-valued surfaces and intensity (magnitude-squared) images. The HG functions form an infinite basis for square-integrable functions, though a sparse set of functions are needed to describe a given polarized PSF. (b) Reweighted HG functions from (a) can be summed to model polarized PSFs. The magnitude-squared of the summed surface gives the final model PSF, showing good agreement with simulated polarized PSF for a transition dipole rotated 20° off-axis.

4.3. ℓ_2-minimization for Hermite-Gaussian fitting

One common method to find the best fit between a model and a target image is to minimize the error (also called the residue) by finding the set of fit parameters that minimize the ℓ_2-norm. I used this method to fit polarized PSFs to the weighted sum of the HG basis, where the weights of the basis functions are the fit parameters. While approximating polarized PSFs from HG functions can be accomplished by visual inspection and trial-and-error, I needed robust fitting algorithm to test the implementation of this basis. Using the ℓ_2-norm of the residue as the objective function to minimize suffices to test this model. For the purpose of developing this fitting method, I represented the HG basis functions as matrices centered and scaled to match the simulated polarized PSFs.

In order to implement the minimization, I first defined the objective function using linear algebra notation. The polarized PSF is reshaped into an $L \times 1$ column vector, X, while the HG bases are also cast as vectors and combined into a $L \times M$ matrix, H, where linear pixel index of an image matrix is mapped to row number. The weights of the basis function $\vec{w}$ is an $M \times 1$ column vector, and the goal of the minimization is to recover this vector. The vector lengths L and M are the number of pixels in the intensity map (10,000 for a 100×100-pixel image) and the number of HG functions used in the basis, respectively. I included the HG basis functions for mode numbers of 0 to 3 in both dimensions ($M = 16$) since the structure of multi-lobed PSFs I tested doesn't show more than 4 lobes along either Cartesian axis. In the future, extracting lobe positions and relative intensities of PSFs could be used to

initially classify PSFs and choose a smaller subset of basis functions based on that

class.

The expression for the objective function is complicated due to the mismatch

between the positive-real valued PSF and the complex-valued HG basis functions. In

the absence of this mismatch, the residue would be expressed as $\vec{r}(\vec{a}) = \vec{s} - H\vec{w}$. In

fact, due to the orthonormal nature of the HG basis, I would ideally be able to project

the PSF onto the basis to obtain the weight vector. Unfortunately, the use of a

complex-valued basis for positive-real valued image fitting necessitates an extra

step. The fit must be mapped to the positive-real plane by multiplying each element

by its complex conjugate, i.e. the magnitude squared of each element. This element-

wise operation cannot be carried out using standard linear algebra operators, and as

such, must be handled carefully while developing the minimization expression.

Taking the complex nature of the basis into account, the minimization of the

objective function for HG fitting is expressed by $\min_{\vec{w}}\|\vec{r}(\vec{w})\|_2^2 = \min_{\vec{w}}\|\vec{s} - |H\vec{w}|^2\|_2^2$,

where $|H\vec{w}|^2$ is the element-wise magnitude squared of the weighted sum of the HG

basis functions, which I will refer to as the fit vector $\vec{f}(\vec{w})$. Similar to how the critical

values of a function $f(x)$ are found by setting $\frac{d}{dx}f(x) = 0$, finding the minimum of

the objective function starts with setting the gradient equal to zero. When

minimizing a function of a vector and its complex conjugate, the gradient is taken

with respect to the complex conjugate. The gradient of the objective function can be

written as

$$\vec{\nabla}_{\vec{w}^*}\|\vec{r}(\vec{w},\vec{w}^*)\|_2^2 = \vec{\nabla}_{\vec{w}^*}\|\vec{s} - \vec{f}(\vec{w},\vec{w}^*)\|_2^2$$

Equation 4.2

where the residue is the difference in the target vector $\vec{s}$ and fit vector $\vec{f}$, written as explicitly depending on $\vec{w}$ and $\vec{w}^*$, (where * represents complex conjugation).

4.4. Expression for the gradient of the objective function

As the analytic expression of the objective function is the most complex part of the HG fitting algorithm, I have included the derivation below. Taking the gradient of the scalar objective function with respect to the complex conjugate of the HG weight vector $\vec{w}^*$ results in an $M \times 1$ column vector which provides the direction in the space of weights pointing toward the greatest increase in the residue. To aid in the derivation of the gradient expression, I define the ℓth row of the basis matrix H as $\vec{H}(\ell) = [H_{\ell,1}, H_{\ell,2}, \cdots H_{\ell,M}]$ and generate the set of L matrices (size $M \times M$)

$$\mathcal{H}^\ell = \vec{H}(\ell)'\vec{H}(\ell)$$

Equation 4.3

formed by the outer product of $\vec{H}(\ell)$ with its complex conjugate.

Rewriting the fit vector $\vec{f}(\vec{w}, \vec{w}^*)$ using Equation 4.3 results in a form for the fit vector written without the element-wise magnitude squared operation, given by

$$\vec{f}(\vec{w}, \vec{w}^*) = \begin{bmatrix} \vec{w}' \mathcal{H}^1 \vec{w} \\ \vdots \\ \vec{w}' \mathcal{H}^L \vec{w} \end{bmatrix}.$$

Equation 4.4

While the objective function is a scalar, the fit vector is $L \times 1$ as described above. Thus, the gradient of a single element of the fit vector can be written as

$\vec{\nabla}_{\vec{w}^*} f_\ell(\vec{w}, \vec{w}^*) = \mathcal{H}^\ell \vec{w}$. Extrapolating the gradient of each term in the fit vector results in the Jacobian matrix of the fit vector with respect to $\vec{w}^*$. The elements of the Jacobian can be written as $\mathcal{J}_{i,j} = \frac{\partial f_i}{\partial w_j^*} = \mathcal{H}^i_{(j,1 \to M)} \vec{w}$. Each column of the Jacobian corresponds to the partial derivative with respect to each element of $\vec{w}^*$ while the rows correspond to each element of the fit vector, forming an $L \times M$ matrix. Using vector calculus to perform the gradient in Equation 4.2 with the Jacobian results in the expression for the gradient of the objective function for HG fitting:

$$\vec{\nabla}_{\vec{w}^*} \|\vec{r}(\vec{w}, \vec{w}^*)\|_2^2 = 2\mathcal{J}^{\mathrm{T}} \left(\vec{s} - \vec{f}(\vec{w}, \vec{w}^*) \right).$$

Equation 4.5

4.5. Testing of Hermite-Gaussian fitting

As Equation 4.5 cannot be solved analytically, I employed the iterative method of steepest descent algorithm to test it. Briefly, this algorithm starts with an initial guess $\vec{w}_0$ iteratively updates by calculating the gradient at each point and incrementing the weight vector in the direction of negative gradient, similar to a ball rolling down a curved surface (or error landscape), where the height represents the value of the residue. The set of weight used the initiate the algorithm can be thought of as the starting point on the error landscape. While better initial guesses improve convergence time, a greater issue is due to the lack of convexity of this minimization problem. For a given target image some initial weight vectors will converge to incorrect intensity maps. This indicates the potential for local minima in Equation 4.5 where the algorithm may become "stuck". Care must be taken in choice of initial state to ensure proper convergence. An example of convergence to the global minimum and local minimum is shown in Figure 4.3, using an additional LASSO regularization term [69] discussed in the following section.
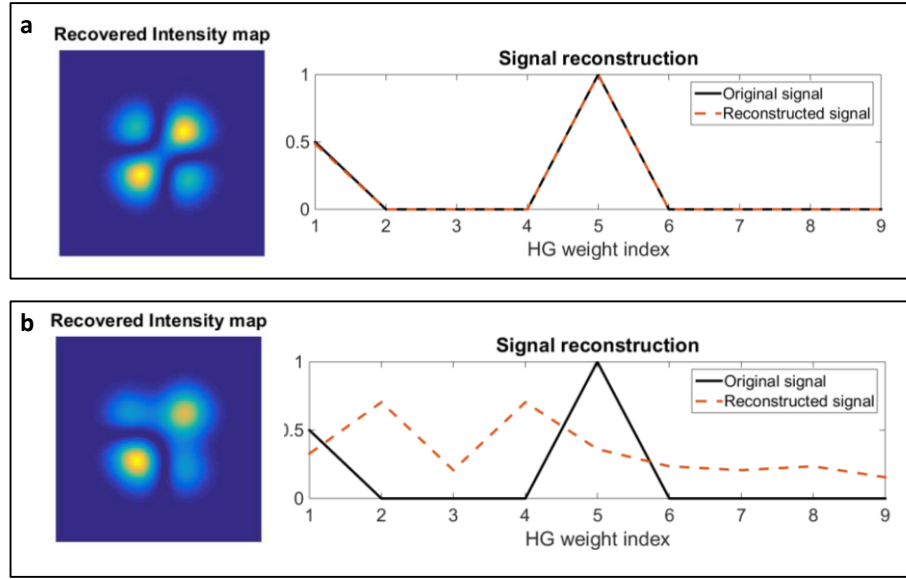
Figure 4.3. Example of results using method of steepest descent algorithm for HG fitting with LASSO regularization. The y-axis of the plots show magnitude of the HG weights as a function of weight index. (a) Successfully recovered HG weights show excellent agreement with the weights used to generate the test image. Reconstructed intensity map appears visually indistinguishable from test image. (b) Example of algorithm converging at a local minima. 4-lobed structure comes from an incorrect, non-sparse set of weights. In this case, LASSO regularization failed to enforce sparsity.

4.6. Using LASSO regression to encourage sparsity

In minimizing Equation 4.5 in an unconstrained fashion, the recovered vector of HG weights, when multiplied by the basis matrix and projected as an intensity map, shows good visual agreement with the test images used when local minima are avoided. However, when compared to the original weights used to generate the test image, it becomes apparent that extra basis functions represent in the reconstruction. As the goal is to recover the true vector of weights for analytic

purposes, the extra non-zero weights are problematic. One solution is to add a regularization term to Equation 4.5 that encourages sparsity, called the least absolute shrinkage and selection operator, or LASSO [69]. The minimization problem with the addition of the LASSO parameter can be written as $\min_{\vec{w}}\|\vec{r}(\vec{w})\|_2^2 = \min_{\vec{w}}\left\||\vec{X} - |H\vec{w}|^2\right\|_2^2 + \lambda\|\vec{w}\|_1$, where $\|\vec{w}\|_1$ is the ℓ_1 norm of the vector of HG weights, and λ is the tunable LASSO parameter. This results in an additional term in the gradient of the objective function,

$$\nabla_{\vec{w}^*}\|\vec{r} + \lambda\|\vec{w}\|_1\|_2^2 = 2J^{\mathrm{T}}\left(\vec{s} - \vec{f}(\vec{w}, \vec{w}^*)\right) + \lambda \cdot SIGN(\vec{w}),$$

Equation 4.6

where $SIGN(\vec{w})$ is the element-wise complex sign of $\vec{w}$. The factor λ can be tuned to change the sparsity of $\vec{w}$.

Substituting Equation 4.6 in place of Equation 4.5 for the method of steepest descent algorithm results in improved sparsity of $\vec{w}$. Figure 4.4 shows the effects of varying the LASSO parameter λ for the same target image and initial state. Under-valued λ still gives good image reconstruction despite extra non-zero weights being recovered. Over-valued λ fails to recover the image or the general trend of the weights due to the sparsity over-constraint.
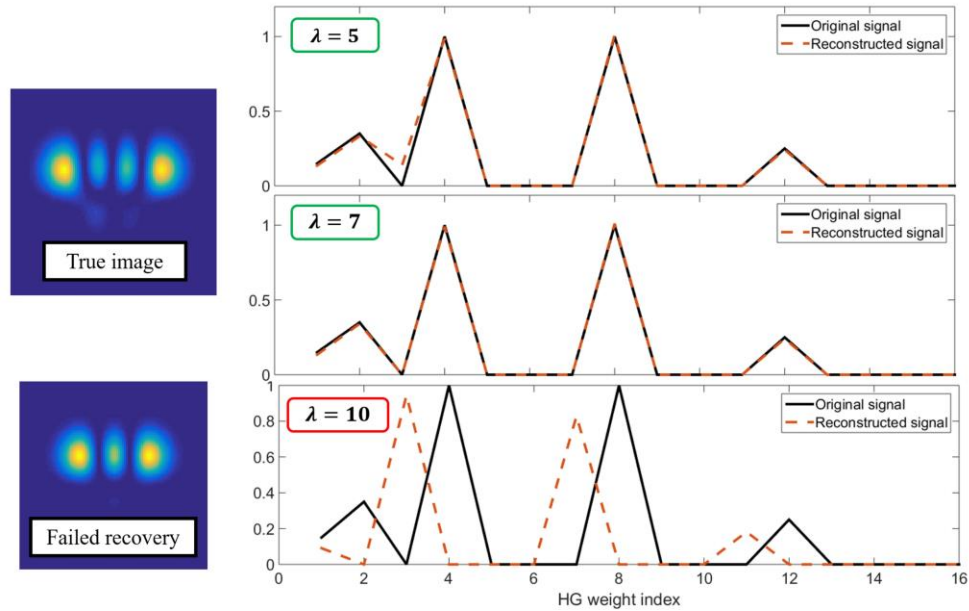
Figure 4.4. Effects of changing LASSO parameter λ. The plots of recovered HG weights versus actual weight are generated for the same test image and the same initial state. Setting λ too low (top plot) reconstructs the intensity map well, but results in extra non-zero weights when compared to the middle plot. When λ is set too high, as in the bottom plot, the algorithm converges to an incorrect set of weights to fulfill the sparsity constraint.

4.7. Implementation of fitting algorithm on simulated PSFs

Having tested the HG fitting algorithm on intensity maps generated from the basis matrix *H*, I applied the fitting algorithm to simulated polarized PSFs as a proof-of-concept. The goal of this test was to determine if fitting simulated PSFs in this manner would yield clear trends of the weights, indicating the potential of this method to recover position and orientation in experimental data. The PSFs used for this test were simulated in Lumerical FDTD solutions for a dipole emitter located above the apex of the NW, oriented in-plane and rotated about the optical axis in

increments of 5° starting parallel to the NW axis. The simulation of these PSFs resulted in centered images, and the size of the HG basis to be used was determined manually. In future work, these steps will be automated using aggregate data to simulate experimental conditions. The target images for the fitting algorithm were the normalized PSFs, and the initial state of the weight vector was chosen based on visual confirmation of the accuracy of reconstructed intensity maps.

The reconstructed intensity maps showed visual agreement with the target intensity maps as shown in Figure 4.5, while the recovered weight vectors had four or fewer non-zero weights of the 9 HG modes used in the basis. The magnitude of the error shown in Figure 4.5 are show higher-frequency features with low intensities, which are likely to be negligible in the presence of noise.
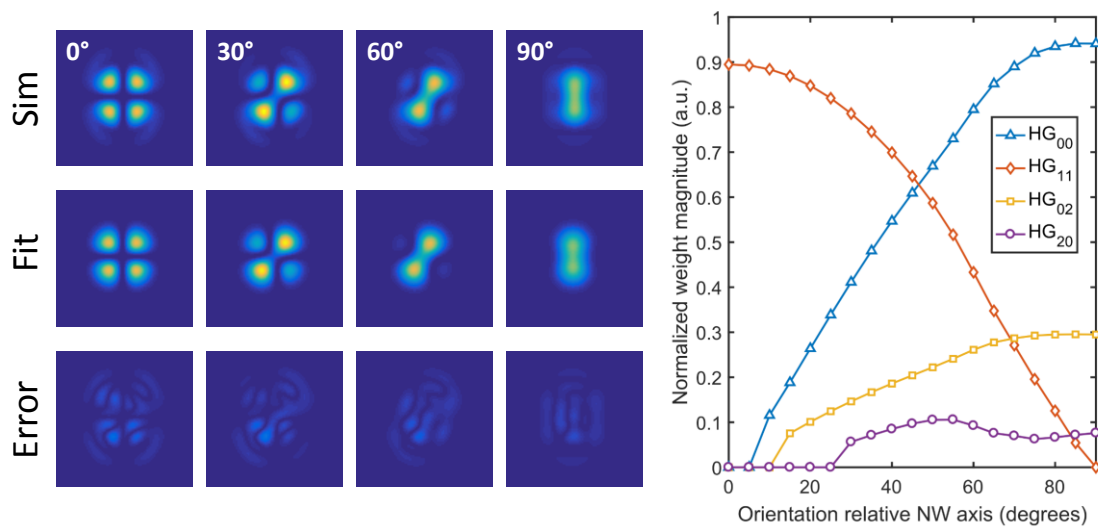
Figure 4.5. Simulated PSFs and results of fitting for transition dipole rotated from 0° to 90° from NW axis. Simulated PSFs, resultant fit, and error are shown for 4 represenative dipole angles. Plot shows the magnitude of the weight vector that minimizes the error as the dipole is rotated about the optical axis.

The magnitudes of the four non-zero weights are plotted in Figure 4.5. The (0,0) and (1,1) HG modes have the greatest effect on PSF shape, with the (1,1) mode responsible for the four-lobed shape, while the (0,0) mode modulates the maximum intensity of the lobed structures in the higher-order HG functions. The smooth variation in weights presented in Figure 4.5 suggest that HG fitting has the potential to recover orientation data from. If the transformation from the set of NW-emitter complex parameters (e.g. NW diameter, dipole emitter position and orientation) to the set of fit parameters (HG weights) can be inverted, this would provide a method for estimating the orientation of dipole emitters on plasmonic NWs.

Chapter 5

Conclusion and Future Work

5.1. Conclusion

In this thesis, I have analyzed simulated and experimental PSFs of dipole emitters near pentagonal cross-section Ag NWs and determined the optimal range of NW diameters to enable the classification of multi-lobed PSFs. I demonstrated that the fluorescence PSFs formed near dye-labeled Ag NWs present a unique set of challenges due to the biasing of single-lobed emitters and the extra localizations from multi-lobed emitters. Simulated PSFs for uniformly distributed dipole emitters for various NW diameters resulted in apparent widths lower than seen in experiment for small NW diameters due to the over-expression of single-lobed PSFs. Due to the decreasing localization bias for smaller NWs, the range of simulated PSFs

were unable to account for the larger apparent width experimentally observed for a ~200 nm diameter NW.

The larger apparent width overestimation for bi-lobed PSFs on thinner NWs predicts that the relative fraction of bi-lobed PSFs is larger than seen through uniform sampling of dipole emitters, most likely due to preferential excitation and binding at the NW edges. This has positive implications for future experiments, as relative weight and separation between the lobes of bi-lobed PSFs provide more encoded information than a single-lobed PSF. As an example of the extra information available from bi-lobed PSFs, I developed and implemented a PSF model based on the HG functions, where the angle of rotation can be related to the relative weights of different beam modes to the polarized PSF. Future research under similar experimental conditions should focus on NW diameters between 200 and 300 nm to enable filtering of bi-lobed PSFs by lobe separation. These multi-lobed PSFs provide a novel system to develop superlocalization techniques that are compatible with plasmonic nanostructures. Improving the viability of superlocalization of events on plasmonic nanostructures will open the door to optically measure surface activity in nanocatalyst development in the future.

5.2. Future work

In uncovering the different spatial distribution of single- and bi-lobed PSFs for thinner NWs, I've identified a range of NW diameters that future experiments

could use to better understand multi-lobed PSFs. While this work has focused on Ag NWs, Au NWs provide another plasmonic system to study. Using these simulation techniques, I would like to determine the optimal dimensions for isolating bi-lobed PSFs on Au NWs. My preliminary simulations seen in Figure 5.1 show that Au NWs with a trapezoidal cross-section, mimicking lithographically prepared NWs, also support multi-lobed PSF formation. With the ability to precisely define NW dimensions and generate lithographic arrays, a large number of experimental PSFs can be collected and analyzed using my HG fitting method.
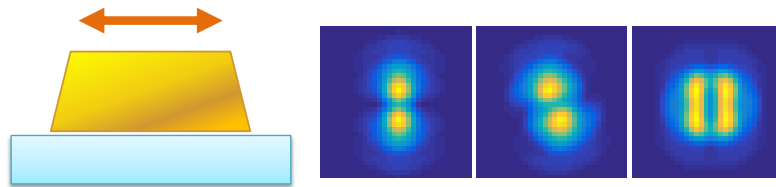
Figure 5.1. Simulated PSFs for dipole source on top of a trapezoidal cross-section Au NW shows multi-lobed characteristics.

This thesis and publications like it focus on quantifying the effects that plasmonic particles have on PSFs and their localization with the goal of minimizing bias and enabling accurate superlocalization of emitters. Fitting PSFs also quantifies the far field representation of what is happening inside of plasmonic particles. In this thesis I have investigated the far field expression of the plasmonic nanoantenna effect on dye molecules, but my future work will look more closely at how plasmon mode structure modulates coupling, scattering, and absorption. Collaborators in the

Link lab have discovered spatially-dependent absorption and scattering in Au plasmonic nanostructures. Long Au nanorods (~500 nm) show wavelength-dependent photothermal PSFs that can be spread out over the nanorod, focused on the ends, or focused in the middle. Au nanorings have shown asymmetric scattering PSFs based on the handedness of circularly polarized excitation light. These newly discovered phenomena could lead to better localized heating or tunable scattering structures, but still need quantification and theory to understand. Characterization of PSFs and simulation of plasmon mode structure and current density inside the particles will provide much needed insights and enable the optimization of these nanostructures.

References

1.   J. Grunes, J. Zhu, and G. A. Somorjai, "Catalysis and nanoscience," Chem Commun (Camb), 2257-2260 (2003).
2.   S. Mukherjee, F. Libisch, N. Large, O. Neumann, L. V. Brown, J. Cheng, J. B. Lassiter, E. A. Carter, P. Nordlander, and N. J. Halas, "Hot electrons do the impossible: plasmon-induced dissociation of H2 on Au," Nano Lett **13**, 240-247 (2013).
3.   G. Baffou, and R. Quidant, "Nanoplasmonics for chemistry," Chem Soc Rev **43**, 3898-3907 (2014).
4.   S. Linic, U. Aslam, C. Boerigter, and M. Morabito, "Photochemical transformations on plasmonic metal nanoparticles," Nat Mater **14**, 567-576 (2015).
5.   A. E. Schlather, A. Manjavacas, A. Lauchner, V. S. Marangoni, C. J. DeSantis, P. Nordlander, and N. J. Halas, "Hot Hole Photoelectrochemistry on Au@SiO2@Au Nanoparticles," J Phys Chem Lett **8**, 2060-2067 (2017).
6.   S. Lal, S. Link, and N. J. Halas, "Nano-optics from sensing to waveguiding," Nature Photonics **1**, 641-648 (2007).
7.   M. L. Brongersma, N. J. Halas, and P. Nordlander, "Plasmon-induced hot carrier science and technology," Nat Nanotechnol **10**, 25-34 (2015).
8.   A. Marimuthu, J. Zhang, and S. Linic, "Tuning selectivity in propylene epoxidation by plasmon mediated photo-switching of Cu oxidation state," Science **339**, 1590-1593 (2013).
9.   P. Christopher, H. Xin, and S. Linic, "Visible-light-enhanced catalytic oxidation reactions on plasmonic silver nanostructures," Nat Chem **3**, 467-472 (2011).
10.   D. F. Swearer, R. K. Leary, R. Newell, S. Yazdi, H. Robatjazi, Y. Zhang, D. Renard, P. Nordlander, P. A. Midgley, N. J. Halas, and E. Ringe, "Transition-Metal Decorated Aluminum Nanocrystals," ACS Nano **11**, 10281-10288 (2017).
11.   D. F. Swearer, H. Zhao, L. Zhou, C. Zhang, H. Robatjazi, J. M. Martirez, C. M. Krauter, S. Yazdi, M. J. McClain, E. Ringe, E. A. Carter, P. Nordlander, and N. J. Halas, "Heterometallic antenna-reactor complexes for photocatalysis," Proc Natl Acad Sci U S A **113**, 8916-8920 (2016).
12.   C. Zhang, H. Zhao, L. Zhou, A. E. Schlather, L. Dong, M. J. McClain, D. F. Swearer, P. Nordlander, and N. J. Halas, "Al-Pd Nanodisk Heterodimers as Antenna-Reactor Photocatalysts," Nano Lett **16**, 6677-6682 (2016).
13.   K. Wu, J. Chen, J. R. McBride, and T. Lian, "Efficient hot-electron transfer by a plasmon-induced interfacial charge-transfer transition," Science **349**, 632-635 (2015).
14.   Y. Tian, and T. Tatsuma, "Mechanisms and applications of plasmon-induced charge separation at TiO2 films loaded with gold nanoparticles," Journal of the American Chemical Society **127**, 7632-7637 (2005).
15.   J. T. Li, S. K. Cushing, P. Zheng, T. Senty, F. K. Meng, A. D. Bristow, A. Manivannan, and N. Q. Wu, "Solar Hydrogen Generation by a CdS-Au-TiO2 Sandwich

Nanorod Array Enhanced with Au Nanoparticle as Electron Relay and Plasmonic Photosensitizer," Journal of the American Chemical Society **136**, 8438-8449 (2014).

16. S. Mukherjee, L. Zhou, A. M. Goodman, N. Large, C. Ayala-Orozco, Y. Zhang, P. Nordlander, and N. J. Halas, "Hot-electron-induced dissociation of H2 on gold nanoparticles supported on SiO2," J Am Chem Soc **136**, 64-67 (2014).

17. R. Narayanan, and M. A. El-Sayed, "Shape-dependent catalytic activity of platinum nanoparticles in colloidal solution," Nano Letters **4**, 1343-1348 (2004).

18. X. Zhou, N. M. Andoy, G. Liu, E. Choudhary, K. S. Han, H. Shen, and P. Chen, "Quantitative super-resolution imaging uncovers reactivity patterns on single nanocatalysts," Nat Nanotechnol **7**, 237-241 (2012).

19. N. M. Andoy, X. Zhou, E. Choudhary, H. Shen, G. Liu, and P. Chen, "Single-molecule catalysis mapping quantifies site-specific activity and uncovers radial activity gradient on single 2D nanocrystals," J Am Chem Soc **135**, 1845-1852 (2013).

20. L. Su, G. Lu, B. Kenens, S. Rocha, E. Fron, H. Yuan, C. Chen, P. Van Dorpe, M. B. Roeffaers, H. Mizuno, J. Hofkens, J. A. Hutchison, and I. H. Uji, "Visualization of molecular fluorescence point spread functions via remote excitation switching fluorescence microscopy," Nat Commun **6**, 6287 (2015).

21. H. Shen, L. J. Tauzin, R. Baiyasi, W. Wang, N. Moringo, B. Shuang, and C. F. Landes, "Single Particle Tracking: From Theory to Biophysical Applications," Chem Rev **117**, 7331-7376 (2017).

22. A. R. Small, and R. Parthasarathy, "Superresolution localization methods," Annu Rev Phys Chem **65**, 107-125 (2014).

23. A. Small, and S. Stahlheber, "Fluorophore localization algorithms for super-resolution microscopy," Nature methods **11**, 267-279 (2014).

24. K. L. Blythe, E. J. Titus, and K. A. Willets, "Comparing the Accuracy of Reconstructed Image Size in Super-Resolution Imaging of Fluorophore-Labeled Gold Nanorods Using Different Fit Models," J Phys Chem C **119**, 19333-19343 (2015).

25. L. Su, H. Yuan, G. Lu, S. Rocha, M. Orrit, J. Hofkens, and H. Uji-i, "Super-resolution Localization and Defocused Fluorescence Microscopy on Resonantly Coupled Single-Molecule, Single-Nanorod Hybrids," ACS Nano **10**, 2455-2466 (2016).

26. T. H. Taminiau, F. D. Stefani, F. B. Segerink, and N. F. Van Hulst, "Optical antennas direct single-molecule emission," Nature Photonics **2**, 234-237 (2008).

27. A. S. De Silva Indrasekara, B. Shuang, F. Hollenhorst, B. S. Hoener, A. Hoggard, S. Chen, E. Villarreal, Y. Y. Cai, L. Kisley, P. J. Derry, W. S. Chang, E. R. Zubarev, E. Ringe, S. Link, and C. F. Landes, "Optimization of Spectral and Spatial Conditions to Improve Super-Resolution Imaging of Plasmonic Nanoparticles," J Phys Chem Lett **8**, 299-306 (2017).

28. M. Fernandez-Suarez, and A. Y. Ting, "Fluorescent probes for super-resolution imaging in living cells," Nat Rev Mol Cell Biol **9**, 929-943 (2008).

29. M. Bates, B. Huang, G. T. Dempsey, and X. Zhuang, "Multicolor super-resolution imaging with photo-switchable fluorescent probes," Science **317**, 1749-1753 (2007).

30.   B. Huang, H. Babcock, and X. Zhuang, "Breaking the diffraction barrier: super-resolution imaging of cells," Cell **143**, 1047-1058 (2010).

31.   C. Manzo, T. S. van Zanten, S. Saha, J. A. Torreno-Pina, S. Mayor, and M. F. Garcia-Parajo, "PSF decomposition of nanoscopy images via Bayesian analysis unravels distinct molecular organization of the cell membrane," Scientific reports **4**, 4354 (2014).

32.   L. Schermelleh, R. Heintzmann, and H. Leonhardt, "A guide to super-resolution fluorescence microscopy," J Cell Biol **190**, 165-175 (2010).

33.   H. Cang, A. Labno, C. Lu, X. Yin, M. Liu, C. Gladden, Y. Liu, and X. Zhang, "Probing the electromagnetic field of a 15-nanometre hotspot by single molecule imaging," Nature **469**, 385-388 (2011).

34.   C. Rocker, M. Potzl, F. Zhang, W. J. Parak, and G. U. Nienhaus, "A quantitative fluorescence study of protein monolayer formation on colloidal nanoparticles," Nat Nanotechnol **4**, 577-580 (2009).

35.   X. Zhou, W. Xu, G. Liu, D. Panda, and P. Chen, "Size-dependent catalytic activity and dynamics of gold nanoparticles at the single-molecule level," J Am Chem Soc **132**, 138-146 (2010).

36.   W. L. Xu, H. Shen, G. K. Liu, and P. Chen, "Single-Molecule Kinetics of Nanoparticle Catalysis," Nano Research **2**, 911-922 (2009).

37.   K. S. Han, G. Liu, X. Zhou, R. E. Medina, and P. Chen, "How does a single Pt nanocatalyst behave in two different reactions? A single-molecule study," Nano Lett **12**, 1253-1259 (2012).

38.   P. Anger, P. Bharadwaj, and L. Novotny, "Enhancement and quenching of single-molecule fluorescence," Phys Rev Lett **96**, 113002 (2006).

39.   H. Lin, S. P. Centeno, L. Su, B. Kenens, S. Rocha, M. Sliwa, J. Hofkens, and H. Uji-i, "Mapping of surface-enhanced fluorescence on metal nanoparticles using super-resolution photoactivation localization microscopy," Chemphyschem **13**, 973-981 (2012).

40.   M. J. Rust, M. Bates, and X. Zhuang, "Sub-diffraction-limit imaging by stochastic optical reconstruction microscopy (STORM)," Nat Methods **3**, 793-795 (2006).

41.   E. Betzig, G. H. Patterson, R. Sougrat, O. W. Lindwasser, S. Olenych, J. S. Bonifacino, M. W. Davidson, J. Lippincott-Schwartz, and H. F. Hess, "Imaging intracellular fluorescent proteins at nanometer resolution," Science **313**, 1642-1645 (2006).

42.   R. Jungmann, C. Steinhauer, M. Scheible, A. Kuzyk, P. Tinnefeld, and F. C. Simmel, "Single-molecule kinetics and super-resolution microscopy by fluorescence imaging of transient binding on DNA origami," Nano Lett **10**, 4756-4761 (2010).

43.   J. X. Chen, A. Bremauntz, L. Kisley, B. Shuang, and C. F. Landes, "Super-Resolution mbPAINT for Optical Localization of Single-Stranded DNA," Acs Applied Materials & Interfaces **5**, 9338-9343 (2013).

44.   R. Parthasarathy, "Rapid, accurate particle tracking by calculation of radial symmetry centers," Nat Methods **9**, 724-726 (2012).

45.   S. Ram, E. S. Ward, and R. J. Ober, "Beyond Rayleigh's criterion: a resolution measure with application to single-molecule microscopy," Proc Natl Acad Sci U S A **103**, 4457-4462 (2006).

46.   B. Zhang, J. Zerubia, and J.-C. Olivo-Marin, "Gaussian approximations of fluorescence microscope point-spread function models," Applied Optics **46**, 1819-1829 (2007).

47.   M. Raab, C. Vietz, F. D. Stefani, G. P. Acuna, and P. Tinnefeld, "Shifting molecular localization by plasmonic coupling in a single-molecule mirage," Nat Commun **8**, 13966 (2017).

48.   K. L. Blythe, E. J. Titus, and K. A. Willets, "Effects of Tuning Fluorophore Density, Identity, and Spacing on Reconstructed Images in Super-Resolution Imaging of Fluorophore-Labeled Gold Nanorods," J Phys Chem C **119**, 28099-28110 (2015).

49.   E. A. Wertz, B. P. Isaacoff, and J. S. Biteen, "Wavelength-Dependent Super-resolution Images of Dye Molecules Coupled to Plasmonic Nanotriangles," Acs Photonics **3**, 1733-1740 (2016).

50.   K. A. Willets, A. J. Wilson, V. Sundaresan, and P. B. Joshi, "Super-Resolution Imaging and Plasmonics," Chem Rev **117**, 7538-7582 (2017).

51.   Q. Li, D. Pan, H. Wei, and H. Xu, "Plasmon-Assisted Selective and Super-Resolving Excitation of Individual Quantum Emitters on a Metal Nanowire," Nano Lett (2018).

52.   D. E. Chang, A. S. Sorensen, P. R. Hemmer, and M. D. Lukin, "Quantum optics with surface plasmons," Phys Rev Lett **97**, 053002 (2006).

53.   H. Wei, D. Ratchford, X. E. Li, H. Xu, and C. K. Shih, "Propagating surface plasmon induced photon emission from quantum dots," Nano Lett **9**, 4168-4171 (2009).

54.   Y. Fedutik, V. V. Temnov, O. Schops, U. Woggon, and M. V. Artemyev, "Exciton-plasmon-photon conversion in plasmonic nanostructures," Phys Rev Lett **99**, 136802 (2007).

55.   Q. Li, H. Wei, and H. Xu, "Resolving single plasmons generated by multiquantum-emitters on a silver nanowire," Nano Lett **14**, 3358-3363 (2014).

56.   A. G. Curto, G. Volpe, T. H. Taminiau, M. P. Kreuzer, R. Quidant, and N. F. van Hulst, "Unidirectional emission of a quantum dot coupled to a nanoantenna," Science **329**, 930-933 (2010).

57.   H. Aouani, O. Mahboub, E. Devaux, H. Rigneault, T. W. Ebbesen, and J. Wenger, "Plasmonic antennas for directional sorting of fluorescence emission," Nano Lett **11**, 2400-2406 (2011).

58.   P. B. Johnson, and R. W. Christy, "Optical Constants of the Noble Metals," Physical Review B **6**, 4370-4379 (1972).

59.   L. Novotny, and B. Hecht, *Principles of Nano-Optics* (Cambridge University Press, 2006).

60.   M. Leutenegger, R. Rao, R. A. Leitgeb, and T. Lasser, "Fast focus field calculations," Optics express **14**, 11277-11291 (2006).

61.	G. P. Acuna, F. M. Moller, P. Holzmeister, S. Beater, B. Lalkens, and P. Tinnefeld, "Fluorescence Enhancement at Docking Sites of DNA-Directed Self-Assembled Nanoantennas," Science **338**, 506-510 (2012).

62.	N. S. Abadeer, M. R. Brennan, W. L. Wilson, and C. J. Murphy, "Distance and plasmon wavelength dependent fluorescence of molecules bound to silica-coated gold nanorods," ACS Nano **8**, 8392-8406 (2014).

63.	P. Prabhat, S. Ram, E. S. Ward, and R. J. Ober, "Simultaneous imaging of different focal planes in fluorescence microscopy for the study of cellular dynamics in three dimensions," IEEE Trans Nanobioscience **3**, 237-242 (2004).

64.	B. Huang, W. Wang, M. Bates, and X. Zhuang, "Three-dimensional super-resolution imaging by stochastic optical reconstruction microscopy," Science **319**, 810-813 (2008).

65.	S. R. Pavani, M. A. Thompson, J. S. Biteen, S. J. Lord, N. Liu, R. J. Twieg, R. Piestun, and W. E. Moerner, "Three-dimensional, single-molecule fluorescence imaging beyond the diffraction limit by using a double-helix point spread function," Proc Natl Acad Sci U S A **106**, 2995-2999 (2009).

66.	S. Stallinga, and B. Rieger, "Position and orientation estimation of fixed dipole emitters using an effective Hermite point spread function model," Opt Express **20**, 5896-5921 (2012).

67.	E. Zauderer, "Complex Argument Hermite-Gaussian and Laguerre-Gaussian Beams," J Opt Soc Am A **3**, 465-469 (1986).

68.	Y. Pagani, and W. Nasalski, "Diagonal relations between elegant Hermite-Gaussian and Laguerre-Gaussian beam fields," Opto-Electron Rev **13**, 51-60 (2005).

69.	S. L. Kukreja, J. Löfberg, and M. J. Brenner, "A Least Absolute Shrinkage and Selection Operator (Lasso) for Nonlinear System Identification," IFAC Proceedings Volumes **39**, 814-819 (2006).